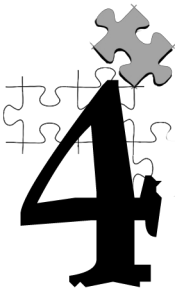

3D radiative transfer simulations of η Carinae's inner colliding winds – II: Ionization structure of helium at periastron

Spectral observations of the massive colliding wind binary Eta Carinae show phase-dependent variations, in intensity and velocity, of numerous helium absorption and emission lines throughout the entire 5.54-yr orbit. Approaching periastron, the 3D structure of the wind–wind interaction region (WWIR) gets highly distorted due to the eccentric ($e \sim 0.9$) orbit. The secondary star ($\eta_{\rm B}$) at these phases is deep within the dense primary's wind photosphere. The combination of these effects are thought to be the cause of the particularly interesting features observed in the helium lines at periastron. We perform 3D radiative transfer simulations of η Car's interacting winds at periastron. We post-process with the SimpleX radiative transfer algorithm 3D smoothed particle hydrodynamics simulations of the inner 150 au of the system, for two different primary star mass-loss rates ($\dot{M}_{\eta_{\rm A}}$). Using previous results from simulations at apastron as guide for the initial conditions, we compute 3D helium ionization maps. We find that, for higher $\dot{M}_{\eta_{\rm A}}$, $\eta_{\rm B}$ He^{0+}-ionizing photons are not able to penetrate into the pre-shock primary wind. He^{+} due to $\eta_{\rm B}$ is only present in a thin layer along the leading arm of the WWIR and in a small region close to the stars. Lowering $\dot{M}_{\eta_{\rm A}}$ allows $\eta_{\rm B}$'s ionizing photons to reach the expanding unshocked secondary wind on the apastron side of the system, and create a low fraction He^{+} in the pre-shock primary wind. With apastron on our side of the system, our results are qualitatively consistent with the observed variations in strength and radial velocity of the helium emission and absorption lines, which helps constrain the regions where these lines arise.

N. Clementel, T. I. Madura, C. J. H. Kruip and J.-P. Paardekooper
submitted to MNRAS

4.1 Introduction

The massive colliding wind binary Eta Carinae (η Car) is one of the most luminous stellar objects in the Galaxy ($L_{\rm Total} \gtrsim 5 \times 10^6$ L$_\odot$). During its highly eccentric ($e \sim 0.9$), 5.54 yr orbit, the slow but high-density wind of the primary star $\eta_{\rm A}$ ($v_\infty \approx 420$ km s^{-1}, $\dot{M}_{\eta_{\rm A}} \approx 8.5 \times 10^{-4}$ M$_\odot$ yr^{-1}; Hillier et al. 2001; Groh et al. 2012a) collides with the faster ($v_\infty \approx 3000$ km s^{-1}; Pittard & Corcoran 2002; Parkin et al. 2009), but less dense ($\dot{M}_{\eta_{\rm B}} \approx 1.4 \times 10^{-5}$ M$_\odot$ yr^{-1}) wind of the secondary star $\eta_{\rm B}$. Every periastron, orbital motion and the binary's large eccentricity highly distort the stellar winds and wind-wind interaction region (WWIR), causing $\eta_{\rm B}$ to become deeply embedded within the denser $\eta_{\rm A}$ wind (Okazaki et al. 2008; Parkin et al. 2011; Madura et al. 2012, 2013). At periastron, the dense distorted $\eta_{\rm A}$ wind and WWIR trap the ionizing radiation from $\eta_{\rm B}$ that is responsible for the formation of numerous high-ionization (ionization potential $\gtrsim$ 13.6 eV) emission and absorption lines observed during the broad part of the orbit around apastron (Verner, Bruhweiler & Gull 2005; Damineli et al. 2008a; Gull et al. 2009, 2011; Madura & Groh 2012; Madura et al. 2012, 2013).

In a recent paper, Clementel et al. (2014b, hereafter Chapter 3) presented results from 3D radiative transfer (RT) simulations focusing on the ionization structure of helium, due to $\eta_{\rm B}$'s ionizing radiation, in the inner $\sim$ 155 au of the η Car system at an orbital phase of apastron. As summarized in Chapter 3, helium spectral features provide important information on both the geometry and physical properties of the η Car binary and the individual stars. While various helium features are present throughout the entire orbit, they show their most interesting behavior during periastron passage (Nielsen et al. 2007; Damineli et al. 2008a; Teodoro et al. 2012).

The goal of this paper is to extend the work of Chapter 3 and analyze the effects of $\eta_{\rm B}$'s ionizing radiation during the spectroscopic low state at periastron. As in Chapter 3, we focus on the inner $\sim$ 155 au of the η Car system and apply the SimpleX RT algorithm (Ritzerveld & Icke 2006; Ritzerveld 2007; Paardekooper, Kruip & Icke 2010; Kruip et al. 2010; Kruip 2011) to 3D smoothed particle hydrodynamics (SPH) simulations of η Car's colliding winds (Madura et al. 2013, hereafter M13) to compute 3D maps of the ionization structure of He. This work sets the stage for future efforts to compute synthetic He line profiles for direct comparison with available observations. The aim is to eventually constrain where and how the observed broad He emission and absorption lines form during the periastron event. We further aim to explain the temporal behavior of the broad He lines as the η Car system moves from apastron through periastron. Again, we note that we focus solely on interpreting the broad emission and absorption features of He that arise in the stellar winds and WWIRs, and not the narrower ($\lesssim$ 50 km s^{-1}) features that form in the Weigelt blobs and other dense, slow-moving near-equatorial circumstellar ejecta (Weigelt & Ebersberger 1986; Damineli et al. 2008a).

The rest of this paper is organized as follows. In Section 4.2, we summarize our numerical approach. Section 4.3 describes the results. A discussion of the results and their implications is in Section 4.4. Section 4.5 summarizes our conclusions and outlines the

direction of future work.

4.2 Methods

The numerical approach in this paper, both for the SPH and RT simulations, are identical to those in Chapter 3. As in previous works, we use the SimpleX algorithm (Ritzerveld & Icke 2006; Ritzerveld 2007; Paardekooper, Kruip & Icke 2010; Kruip et al. 2010; Kruip 2011) to post-process 3D SPH simulation output (M13). For further details, we refer the reader to Chapters 2 and 3 and references therein. We also retain the naming convention used in M13, and Chapters 2 and 3 when referring to the SPH and SimpleX simulations in this paper, namely, Case A ($\dot{M}_{\eta_A} = 8.5 \times 10^{-4}$ $M_\odot\,yr^{-1}$), Case B ($\dot{M}_{\eta_A} = 4.8 \times 10^{-4}$ $M_\odot\,yr^{-1}$), and Case C ($\dot{M}_{\eta_A} = 2.4 \times 10^{-4}$ $M_\odot\,yr^{-1}$). In the following, we briefly describe only the key aspects and differences that are directly relevant to this work.

Due to the high eccentricity of the η Car system ($e \sim 0.9$), as the stars approach periastron, both the 3D structure and the dynamical evolution of the individual stellar winds and WWIR change drastically, compared to the majority of the orbital period. The stellar separation drops to ~ 1.5 au and orbital speeds increase greatly, becoming comparable to the wind speed of η_A (see Section 4.3 for details). The rapid orbital motion during periastron thus leads to major changes in the structure of the winds and WWIR on relatively short time-scales of the order of a few days (Okazaki et al. 2008; Parkin et al. 2011; Madura et al. 2012; M13).

To properly resolve this complex situation, we use two different SPH simulation domain sizes from M13. The larger domain is the same as the one used in Chapters 3 ($r = 10\,a = 155$ au), and allows for a direct comparison of the results in this paper with those at apastron in Chapters 3. The smaller domain simulations have a computational domain radius $r = 1.5\,a = 23$ au and eight times the number of SPH particles used in the $r = 10\,a$ simulations, leading to a roughly factor of two improvement in the overall spatial resolution compared to the $r = 10\,a$ simulations. The high-resolution simulations also focus only on phases around periastron ($\phi = 0.97$–1.03), with output written every $\Delta\phi \approx 8 \times 10^{-4}$, which is approximately every 1.6 days of the 2024-day orbit. These smaller, higher-resolution simulations ensure that we are adequately resolving the stellar winds and WWIR directly between the stars, as well as any possible WWIR 'collapse' that may affect the escape of η_B's ionizing radiation (M13). The higher resolution $r = 1.5\,a$ simulations are also useful for checking the accuracy of the $r = 10\,a$ results.

We consider the ionization of hydrogen and helium atoms by both collisional- and photoionization, and assume the same abundance by number of He relative to H as Hillier et al. (2001), $n_{He}/n_H = 0.2$. We employ a single photoionizing source located at the position of η_B. As in Chapters 3, we consider η_B to be an O5 giant with $T_{eff} \approx 40{,}000$ K, we assume a total ionizing flux for H and He of 3.58×10^{49} photons s^{-1} (Martins, Schaerer & Hillier 2005), and we use three bins to sample the stellar spectrum, which we approximate

with a black body. The width of each frequency bin is set by the ionization energy of each species. The first bin ranges from the ionization frequency of H^{0+} ($\nu_{H^{0+}} = 3.28 \times 10^{15}$ Hz) to that of He^{0+} ($\nu_{He^{0+}} = 5.93 \times 10^{15}$ Hz), the second from $\nu_{He^{0+}}$ to $\nu_{He^{+}}$ (1.31×10^{16} Hz), and the third from $\nu_{He^{+}}$ to a maximum frequency equal to ten times $\nu_{H^{0+}}$. We use an effective cross-section representation to determine the correct number of absorptions within each frequency bin. We set the black body temperature to the value that produces the correct ratio $\text{photons}_{H^{0+}}/\text{photons}_{He^{0+}}$ (in this case $T_{bb} = 49{,}000$ K), in accordance with the $q_{H^{0+}}/q_{He^{0+}}$ ratio in Martins, Schaerer & Hillier (2005). $q_{He^{+}}$ is effectively zero for η_B.

In figures displaying our SimpleX results for density and temperature, we visualize the average of the four vertices that compose each Delaunay cell. Unfortunately, this approach leads to cell values which are difficult to interpret if the vertex values differ by several orders of magnitude. In our simulations, this might occur for the fractions of He^{0+}, He^{+} and He^{2+}. In order to visualize results for these quantities in an understandable way that more truthfully represents the physics of our RT simulations, we adopt the visualization approach described in Section 3.2.2.5 of Chapters 3. In all figures showing ionization structure, we display the minimum vertex value for the fraction of He^{0+} and the maximum vertex value for the fraction of He^{2+}. For He^{+}, we show the maximum value whenever the temperature of the gas is lower then 10^5 K, and the minimum otherwise (for temperatures $> 10^5$ K, the fraction of He^{+}, due to collisional ionization, is $\approx 10^{-3}$ or lower). For the reasons discussed in section 2.3.1 of Chapters 3, we do not include plots of the ionization structure of H. We emphasize that the visualizations are merely to help guide the reader, and neither the physics nor the conclusions of our work depend on them (see Chapters 3 for details).

Using the method described in Section 3.2.3.1 of Chapters 3, we account for the inner He^{+} volume around η_A ($r \sim 3$ au for Case A, and ~ 7.5 au for Case B) based on 1D cmfgen models of η Car by Hillier et al. (2001, 2006). We do not include the inner He^{2+} zone in η_A's wind in the $r = 10a$ simulations since it is of negligible size ($r < 1$ au), and because η_B produces essentially zero He^{+}-ionizing photons. Due to their smaller domain size, for added accuracy, the 23 au simulations do include the He^{2+} structure in η_A's innermost wind ($r \sim 0.7$ au for Case A, and ~ 0.8 au for Case B).

As discussed in Chapters 3, our results at apastron appear to rule out low values of $\dot{M}_{\eta_A}$, such as that in Case C. This is supported by the work of M13 and recent observations of η Car (T. Gull and M. Corcoran, private communication). Therefore, we focus in this paper on simulation Cases A and B, which more likely represent η_A's current mass loss rate. Moreover, little information would be obtained by including Case C since for such a low mass loss rate η_A already singly-ionizes He throughout the entire computational domain in the $r = 1.5a$ simulations, and nearly the entire domain (out to $r \approx 120$ au) in the $r = 10a$ simulations.

Finally, we note that we use a standard Cartesian coordinate system with the origin located at the system centre of mass and the orbital plane set in the xy plane, with the major axis along the x-axis. The stars orbit counterclockwise if viewed from along the $+z$-axis. In this system of reference, at periastron, η_A is to the right and η_B is to the left.

4.2.1 Initial ionization state of the gas

As in Chapters 3, we post-process the SPH snapshots. This approach works well for the η Car system at apastron, when the ionization state reaches an equilibrium value on a time-scale much shorter than the orbital time-scale. More importantly, at apastron the $\eta_{\rm B}$ wind cavity is an almost axisymmetric cone, allowing $\eta_{\rm B}$'s ionizing photons to completely ionize the low-density secondary wind. In other words, it is reasonable at apastron to assume that knowledge of the ionization structure of the preceding SPH snapshot is not required for accurate RT results.

In this paper, however, we deal with phases at periastron where, due to rapid orbital motion, the interacting wind structures evolve on a time-scale comparable to the time necessary for the RT simulations to reach a stable ionization state. Moreover, the $\eta_{\rm B}$ wind cavity at periastron is strongly asymmetrical and distorted. Regions that were ionized by $\eta_{\rm B}$ in an earlier snapshot may not be reachable by $\eta_{\rm B}$'s photons in the next snapshot. To tackle these issues, we use a slightly different approach than that in Chapters 3.

Using collisional ionization equilibrium, the results of Chapters 3, and estimates for the recombination time of He^+ as a function of gas density and temperature, we are able to better constrain the initial ionization state of the gas for use as an initial condition in our SimpleX simulations. We know that He^{0+} in the cooler ($T \approx 10^4$ K) unshocked gas in the $\eta_{\rm B}$ wind on the apastron side of the system is completely photoionized by $\eta_{\rm B}$ during most of the binary orbit around apastron Chapters 3. Observations with the *Hubble Space Telescope*/Space Telescope Imaging Spectrograph show that numerous high-ionization lines that require $\eta_{\rm B}$'s ionizing flux are present for most of the orbit and do not start to fade until phase $\phi \approx 0.984$ (approximately one month before periastron, Gull et al. 2009; M13). Therefore, we can safely assume that $\eta_{\rm B}$ is able to completely ionize He^{0+} throughout its unshocked wind at least until $\phi \approx 0.985$ (and at least for the length scales of interest here, $r \lesssim 155$ au from the stars). After $\phi \approx 0.985$, $\eta_{\rm B}$ becomes deeply embedded in the dense wind of $\eta_{\rm A}$ and the WWIR becomes so distorted by orbital motion that we can no longer assume that $\eta_{\rm B}$ can efficiently ionize He^{0+} in its cool unshocked wind. If the He in the low-density ($n \lesssim 10^6$) unshocked $\eta_{\rm B}$ gas is no longer photoionized by the star, then, at $T = 10^4$ K, He^+ should recombine on a time-scale $t_{\rm rec} = 42.4$ days or longer. Thus, around periastron, for gas with $T \approx 10^4$ K and $n \approx 10^6$, the recombination time-scale for He^+ becomes about an order of magnitude larger than the orbital time-scale.

Any gas that recombines very slowly compared to the orbital time-scale around periastron poses a potential problem for the accuracy of our RT simulations, mainly because we are post-processing the SPH simulation output. The SPH output contains no information about the previous ionization state of the gas before we start our SimpleX simulations. However, any gas with a low enough recombination rate should remain ionized from one snapshot to next, even though $\eta_{\rm B}$ photons no longer reach that material[1]. Therefore, we should preserve the ionization state of low-recombination-rate gas in the initial condition of our RT simulations.

[1] Of course, this depends on how long it has been since the supply of ionizing photons has been cut off.

The time difference between phase 0.985 and periastron is ≈ 30 days. The recombination time for gas with $T \approx 10^4$ K and $n \approx 10^6$ is about two weeks longer than this. Lower-density cool gas will have even longer recombination times. If we assume that the η_B ionizing flux becomes trapped by η_A's dense wind and the WWIR at $\phi \approx 0.985$, then at periastron, any such low-recombination-rate gas that was initially photoionized by η_B at $\phi \approx 0.985$ should still be ionized.

Therefore, to mimic the fact that the low-density, cool η_B wind on the apastron side of the system should remain ionized at periastron, we set the He fractions in the η_B wind material with $n < 10^7$ and $T < 4 \times 10^4$ K to be $\sim 97\%$ He^+. This should generate an initial condition closer to the previous ionizations state of the photoionized η_B gas. For gas with $n < 10^7$ and $T < 4 \times 10^4$ K, the recombination time-scale is ≈ 4 days or longer. The use of collisional ionization equilibrium as an initial condition for the remaining gas remains a valid approximation even around periastron, since for the pre- and post-shock η_A wind, the high densities allow the gas to recombine almost instantaneously. Hot ($T > 4 \times 10^4$ K) gas in the post-shock η_B wind will be collisionally ionized to He^+ or higher.

Due to the shorter dynamical time-scales around periastron, which alter the gas distribution from snapshot to snapshot, we must also run SimpleX for a much shorter simulation time, compared to that used at apastron in Chapters 3. In our simulation testing we find that, setting the initial condition of the gas as described above, in Case A, the ionization state reaches an equilibrium value in less than one day. In Case B, the gas reaches ionization equilibrium in ∼ 2–3 days. Since significant changes to the gas density and temperature distributions around periastron also occur on a time-scale of ∼ 2–3 days, we use a total RT simulation time of 2.5 days and a simulation time-step of ∼ 5 minutes in order to achieve an accurate RT calculation of the ionization volumes and fractions. At these time-scales, the gas distribution, even around periastron, can be assumed to be roughly constant.

4.3 Results

To help the reader better understand the RT results, we first briefly describe the density and temperature structure in the *xy*, *xz*, and *yz* planes. For more details on the hydrodynamical simulation results, see M13. Figures 4.1 and 4.2 show the number density (top row) and temperature (bottom row) for the 155 au and 23 au Case A simulations, respectively (the green circles in Figure 4.1 mark the domain size of the 23 au simulations). As described in M13, approaching periastron, the orbital speed of η_A relative to η_B increases to a value of ≈ 360 $km\,s^{-1}$, close to η_A's wind speed (420 $km\,s^{-1}$), thus highly distorting the WWIR. The small stellar separation at periastron (∼ 1.5 au) also prevents η_B's wind from reaching its terminal speed before colliding with η_A's wind. Combined with the effects of radiative inhibition by η_A (M13), this leads to a significant slowing of η_B's pre-shock wind, which alters the wind momentum ratio at the WWIR. This decreases the WWIR opening angle and moves the apex of the WWIR closer to η_B. This behaviour

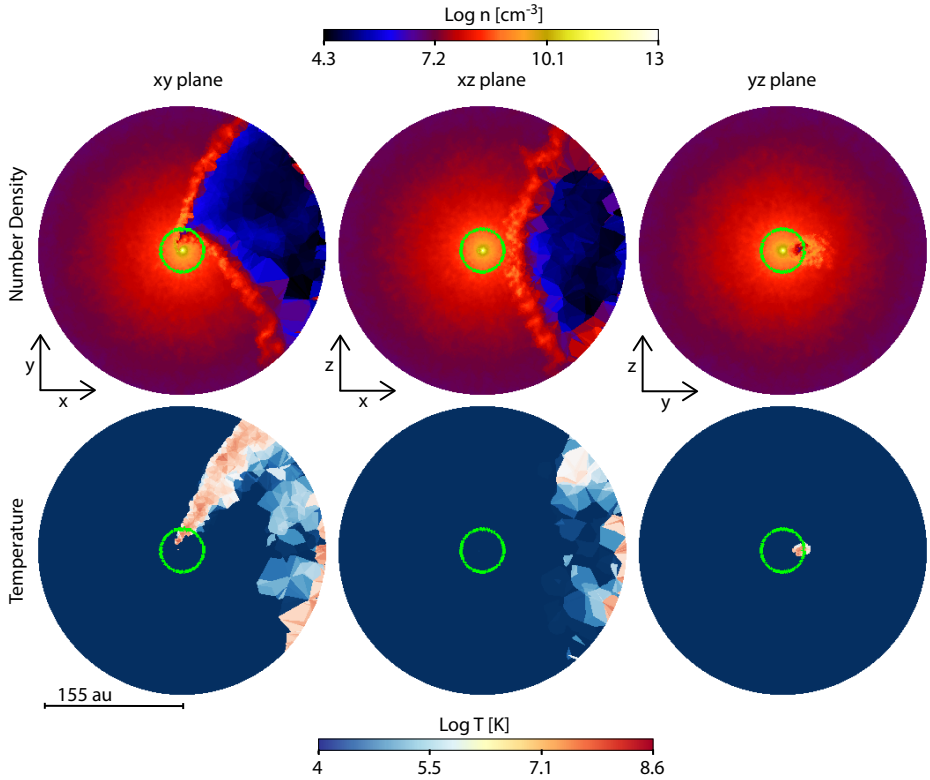

Figure 4.1 – Slices in the *xy* (left-hand column), *xz* (middle column) and *yz* (right-hand column) planes through the larger (10*a*) 3D simulation volume for the Case A simulation at periastron. Top row shows the number density (log scale, cgs units), bottom row shows the temperature (log scale, K). The length scale is shown under the bottom left-hand panel. In the first column (i.e. the orbital plane) η_A is to the right and η_B is to the left. The green circle marks the boundary of the smaller domain simulations (see Figure 4.2).

occurs in the Case B simulations in Figures 4.3 and 4.4 as well, although lowering $\dot{M}_{\eta_A}$ further increases the WWIR opening angle and moves the WWIR apex even closer to η_A.

The above effects create a high asymmetry between the trailing and leading arms of the WWIR at periastron, as η_B becomes deeply embedded in η_A's dense inner wind. The only direction η_B can effectively drive its wind is away from η_A (top left panel of Figures 4.2 and 4.4). This has a strong impact on the location of the shock-heated gas. As shown in the bottom left panel of Figures 4.2 and 4.4, the post-shock secondary wind is heated to temperatures higher than 10^6 K only where the η_B wind collides with the highly distorted leading arm of the WWIR (in red). The trailing wind of η_B is unable to collide with η_A's downstream wind, and so there is no hot shocked gas there. This effect is also visible in the bottom left panel of Figures 4.1 and 4.3. However, some residual hot gas remains at

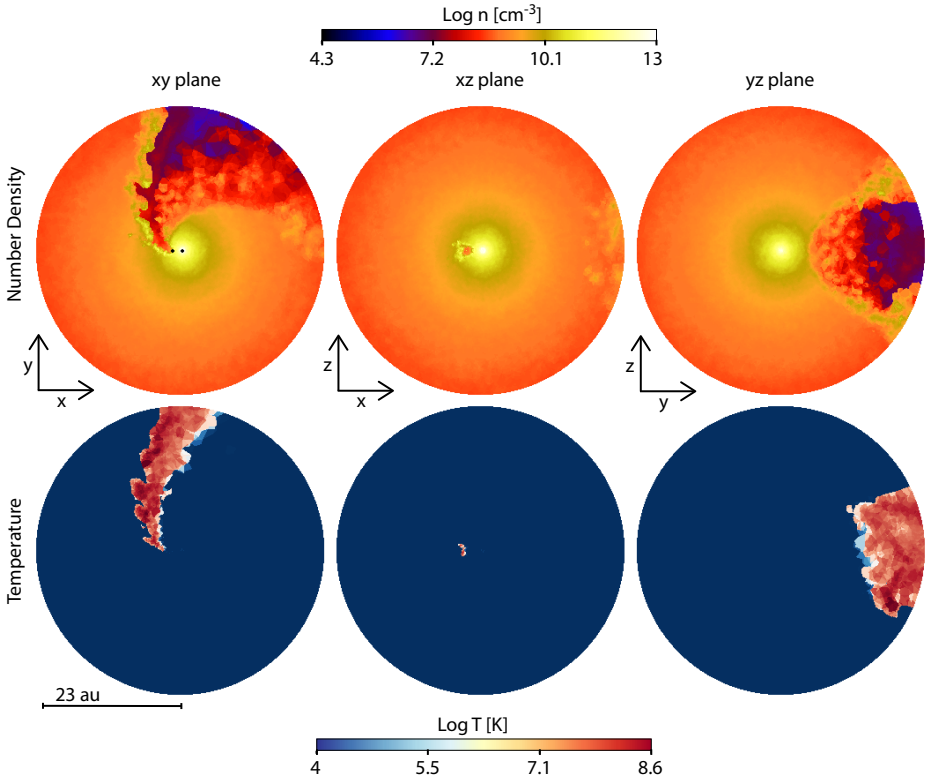

Figure 4.2 – Same as Figure 4.1, but for the smaller (i.e. 1.5 a) simulation domain. The black dots in the center of the top left-hand panel mark the position of the stars.

the outermost right edge of the simulation domain in the xy and xz plane slices. This is the expanding, adiabatically-cooling remnant of the trailing arm of the WWIR from just before periastron.

Looking at the xz plane (middle column of Figures 4.1–4.4), during periastron, $\eta_{\rm B}$ passes behind $\eta_{\rm A}$, allowing, for a short period, the primary wind to expand in the apastron ($+x$) direction. During this time, the apex of the low-density cavity on the apastron side of the system fills with dense primary wind. The thickness and density of this inner primary wind region increases with $\dot{M}_{\eta_{\rm A}}$, since higher $\dot{M}_{\eta_{\rm A}}$ move the apex of the WWIR farther from $\eta_{\rm A}$, allowing the primary wind to fill a larger volume in the apastron direction. Slices in the xz plane also sample mostly cold (10^4 K) gas from both winds, although the $\eta_{\rm B}$ wind cavity in the Case B simulations contains warmer material due to the larger WWIR opening angle and less oblique shocks (M13).

Slices in the yz plane (right-hand column of Figures 4.1–4.4) simply show that at periastron, the leading arm of the WWIR has passed through the yz plane. There are now clear differences in both the density and temperature along the y axis. The $-y$ side of the

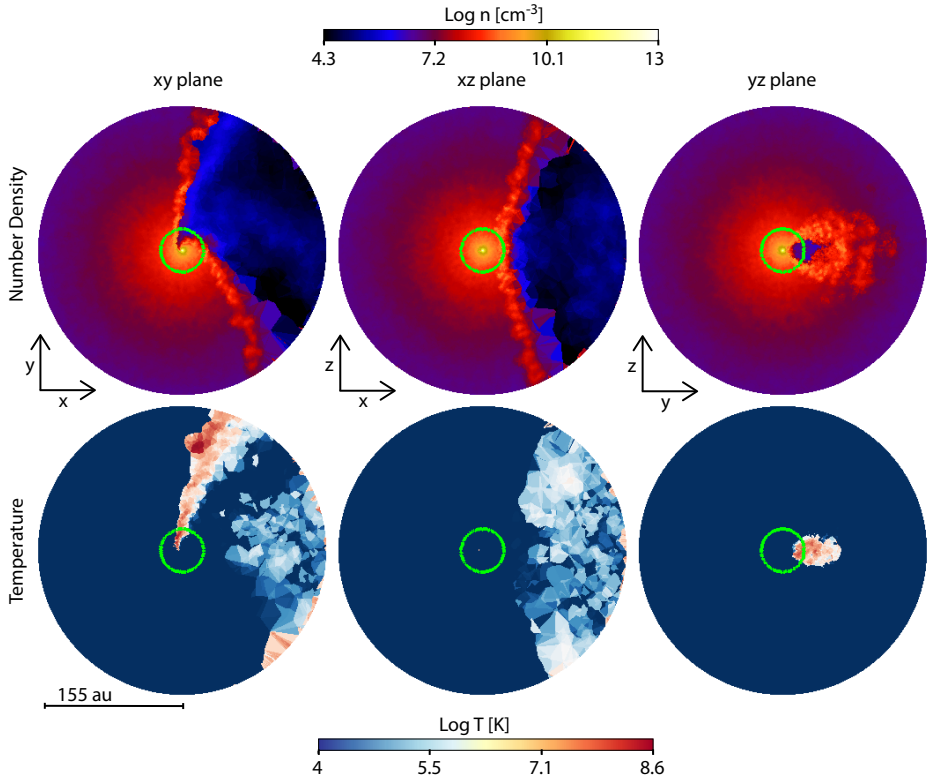

Figure 4.3 – Same as Figure 4.1, but for the Case B simulation.

system still consists of unshocked $\eta_{\rm A}$ wind, but to the $+y$ side there is a small cavity filled with hot, shocked $\eta_{\rm B}$ wind that is bordered by dense post-shock $\eta_{\rm A}$ wind. This cavity is larger in the Case B simulations due to that simulation's larger WWIR opening angle.

4.3.1 Overall He ionization structure and influence of $\dot{M}_{\eta_{\rm A}}$

4.3.1.1 The orbital plane

Figures 4.5 and 4.6 present the He ionization structure in the orbital xy plane for Cases A and B, respectively. Columns illustrate, left to right, the fractions of He^{0+}, He^{+} and He^{2+}. Rows display the 23 au domain without the inner ionization volume due to $\eta_{\rm A}$ (top), the same domain with the inner He^{+} and He^{2+} ionization volumes (middle, filled yellow and blue circles in the left-most panel, respectively), and the larger (155 au) simulation domain with the inner He^{+} ionization volume due to $\eta_{\rm A}$ included (bottom). The green contour highlights the boundary of the unperturbed pre-shock primary wind. Due to the complex situation at periastron, the green contour is meant more as a guide to

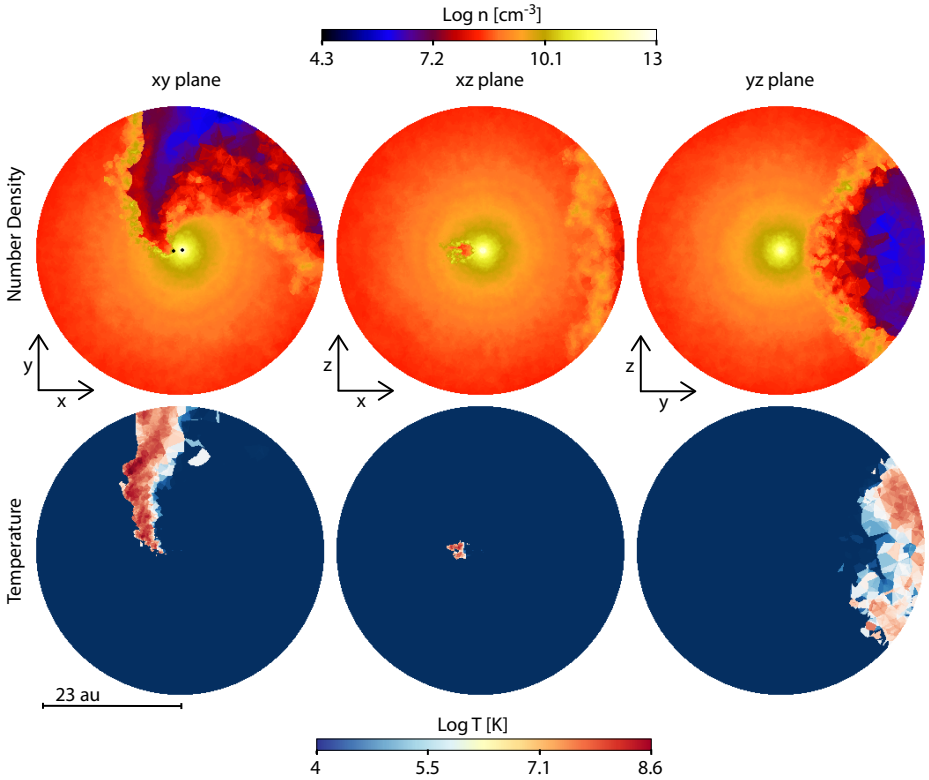

Figure 4.4 – Same as Figure 4.2, but for the Case B simulation.

better understand the results then a precise position for the pre-shock primary wind.

As discussed in Chapters 3, η_B should not have many He^+-ionizing photons and, therefore, He^{2+} is produced principally through collisional ionization. As expected, neglecting the inner He^{2+} region in η_A's wind, He^{2+} is only present in the hottest ($T \gtrsim 10^5$ K) regions of the system, i.e. the shock-heated gas in the leading arm of the WWIR, and the adiabatically-cooling hot gas in the remnant of the trailing arm (from before periastron passage).

Similar to the case at apastron (Chapters 3), η_B ionizing photons create different He^+ structures depending on the value of $\dot{M}_{\eta_A}$. In Case A, the He^{0+}-ionizing photons are only able to ionize a thin layer within the leading arm of the WWIR, and a rather small volume of the diffuse η_A wind that is expanding into the η_B wind cavity located near the remnant of the WWIR's trailing arm (first row of Figure 4.5). The dense primary wind expanding into the η_B wind cavity is able to stop η_B's He^{0+}-ionizing photons. The He^+ present in the cooler, unshocked η_B wind on the apastron side of the system is the previously photoionized gas that is slowly recombining. The inclusion of the inner He^+ and He^{2+} regions due to η_A have basically no effect on the larger-scale He ionization structures in

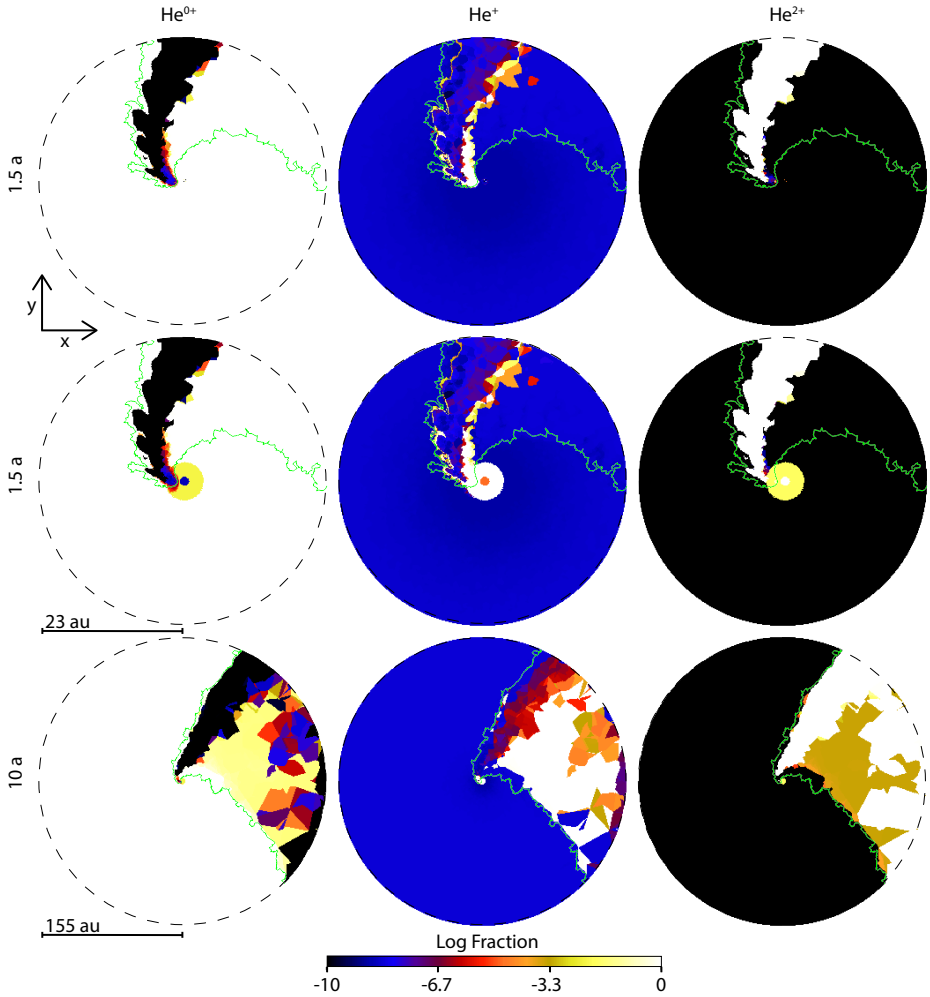

Figure 4.5 – Slices in the orbital plane through the 3D SimpleX simulation volume for the Case A. Column, from left to right show the computed fractions of He^{0+}, He^{+} and He^{2+} (log scale). Rows show,from top to bottom, the smaller (23 au) simulation domain without the inner ionization volumes due to the primary, the smaller (23 au) simulation domain with the He^{+} and He^{2+} inner ionization volumes due to the primary, the bigger (155 au) simulation domain with the He^{+} ionization volume due to the primary. In this and Figure 4.6 the green line marks the edge of the pre-shock primary wind.

Case A (compare the top and middle rows of Figure 4.5). The only noticeable difference is that the He^{0+}-ionizing photons are able to penetrate through the leading arm of the WWIR and further ionize a very small area inside the inner 3 au η_A He^{+} ionization volume (the red within the yellow circle, close to the center in the $-y$ direction in the first panel of the middle row). For Case A the dense outer primary wind, i.e. the area beyond the green contour, is almost entirely He^{0+}.

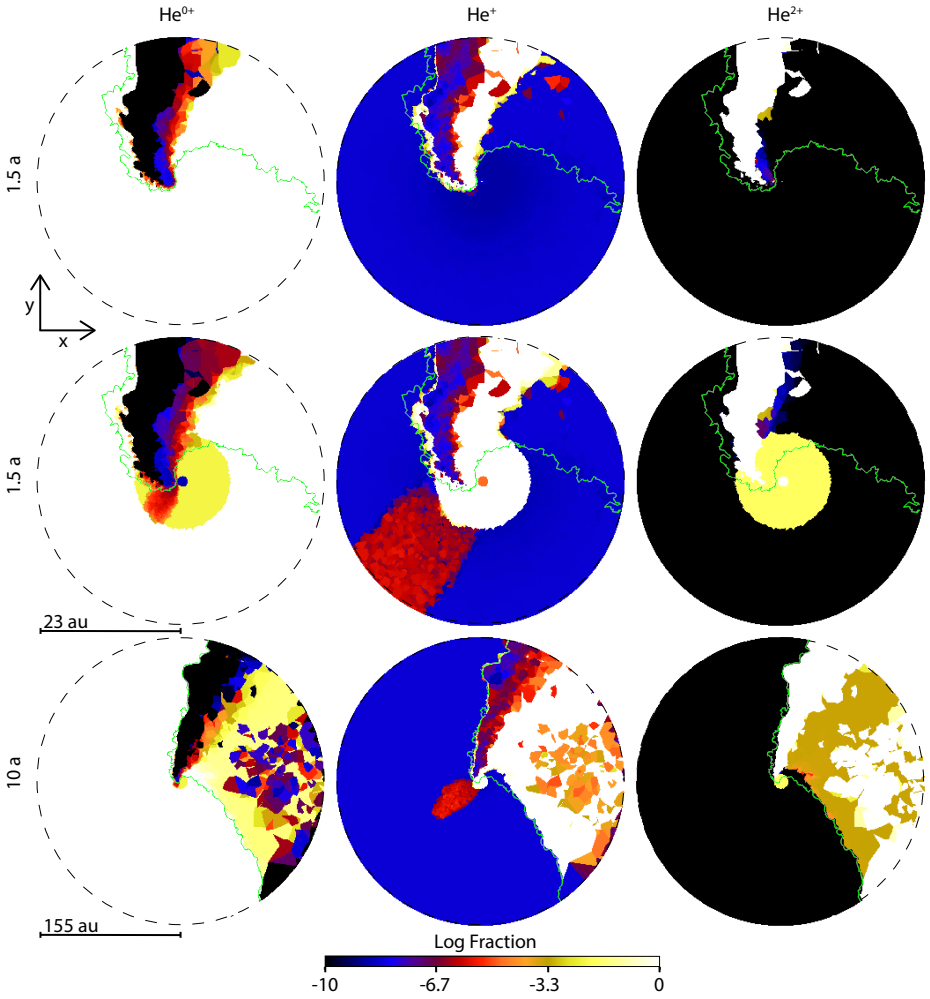

Figure 4.6 – Same as Figure 4.5 but for the Case B.

The larger WWIR opening angle in Case B, due to the lower $\dot{M}_{\eta_A}$, allows the He^{0+}-ionizing photons to escape the inner core and singly-ionize He in a portion of the the expanding primary and secondary winds on the apastron side of the system (right-hand side of the panels in Figure 4.6). Contrary to Case A, introducing the regions of ionized He in η_A's inner wind changes the extent of the ionization front in both the primary and secondary winds. The larger (7.5 au) He^+ zone in Case B allows ionizing photons to penetrate deeper into the receding primary wind, producing a region of He^+ (although the fraction of He^+ remains quite low, see the red region in the middle column in the middle and bottom rows of Figure 4.6). The He^+ on the apastron side of the system is a combination of ongoing photoionization and previously ionized gas which is slowly

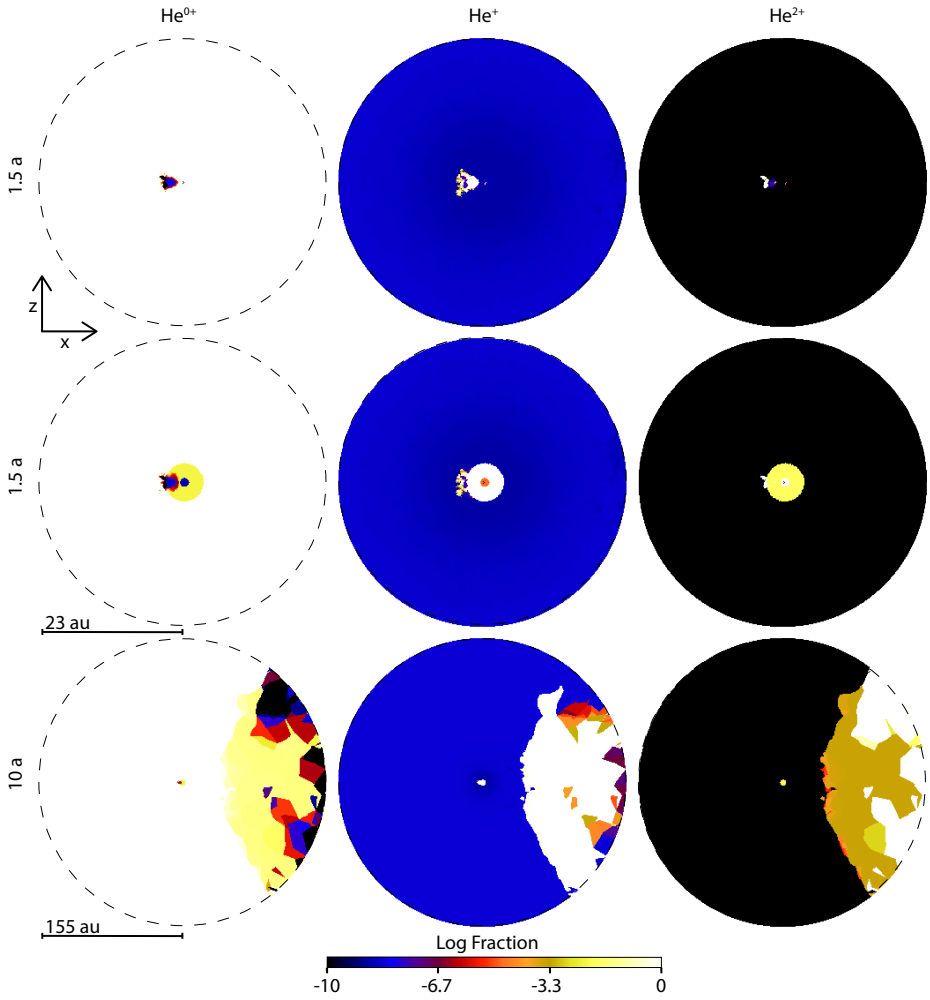

Figure 4.7 – Same as Figure 4.5 but for the *xz* plane.

recombining. However, as in Case A, the dense primary wind is mostly composed of He^{0+} and very effectively traps η_B's He^{0+}-ionizing photons (bottom row of Figure 4.6).

4.3.1.2 The *xz* and *yz* planes

Figures 4.7–4.10 show the ionization fractions in the *xz* and *yz* planes, illustrating the ionization structures below and above the orbital plane. Figures 4.7 and 4.9 further demonstrate that η_A's inner He-ionization zones have no influence on the larger-scale ionization structure in Case A. Again, only Case B shows any clear differences when the η_A He-ionization zones are included.

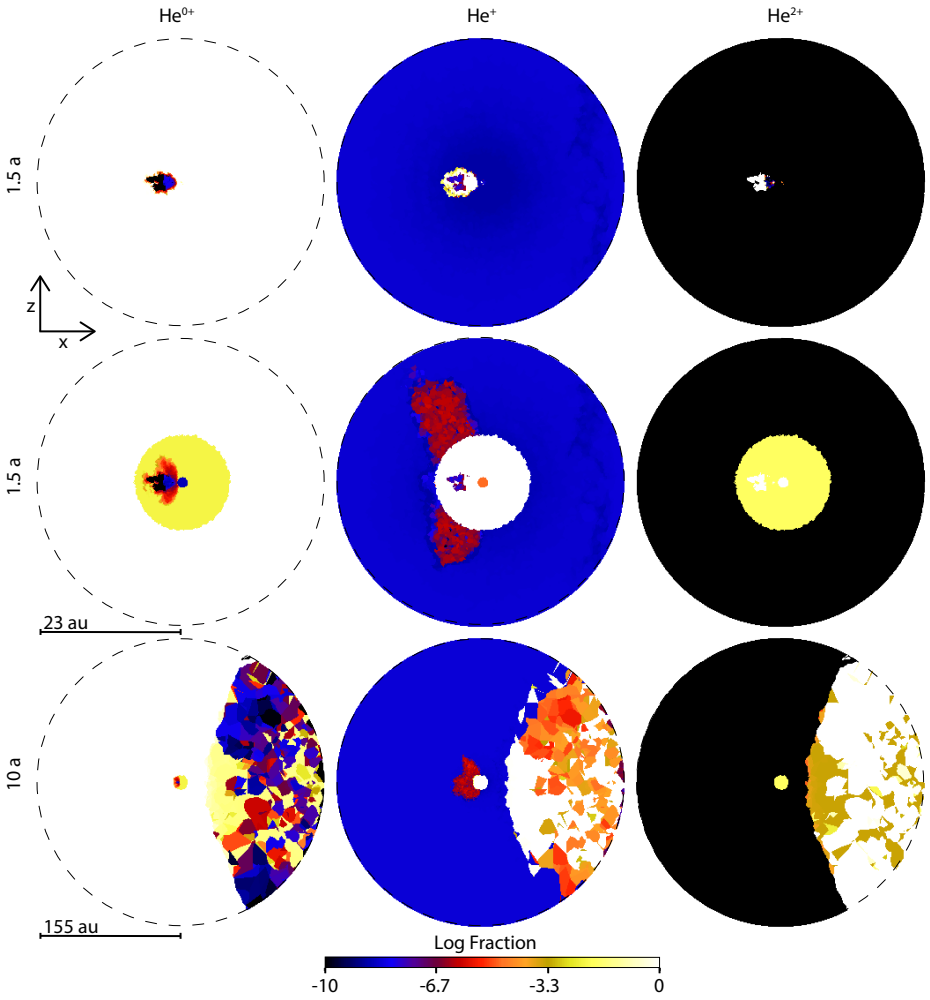

Figure 4.8 – Same as Figure 4.5 but for the Case B *xz* plane.

In the top two rows of Figures 4.7 and 4.8 for the 23 au domain simulations, we see the small central core of He ionization located near the apex of the WWIR in the direction of the leading arm ($-x$ direction). In Case A, there exists only a very small volume of shock-heated gas that is collisionally ionized to He^{2+}, which is bordered by a thin layer of He^{+} that arises due to photoionization of the post-shock η_A wind by η_B. A similar situation occurs in Case B, although again the larger η_A He^{+} zone allows some η_B He^{0+}-ionizing photons to penetrate into the dense primary wind above and below the orbital plane (areas in red in the central panel of Figure 4.8). However, as before, the fraction of He^{+} in these areas is extremely low ($\lesssim 10^{-6}$), so He in the dense η_A wind remains effectively neutral. We see in the bottom row of Figures 4.7 and 4.8 that in both Cases A and B, the hot gas

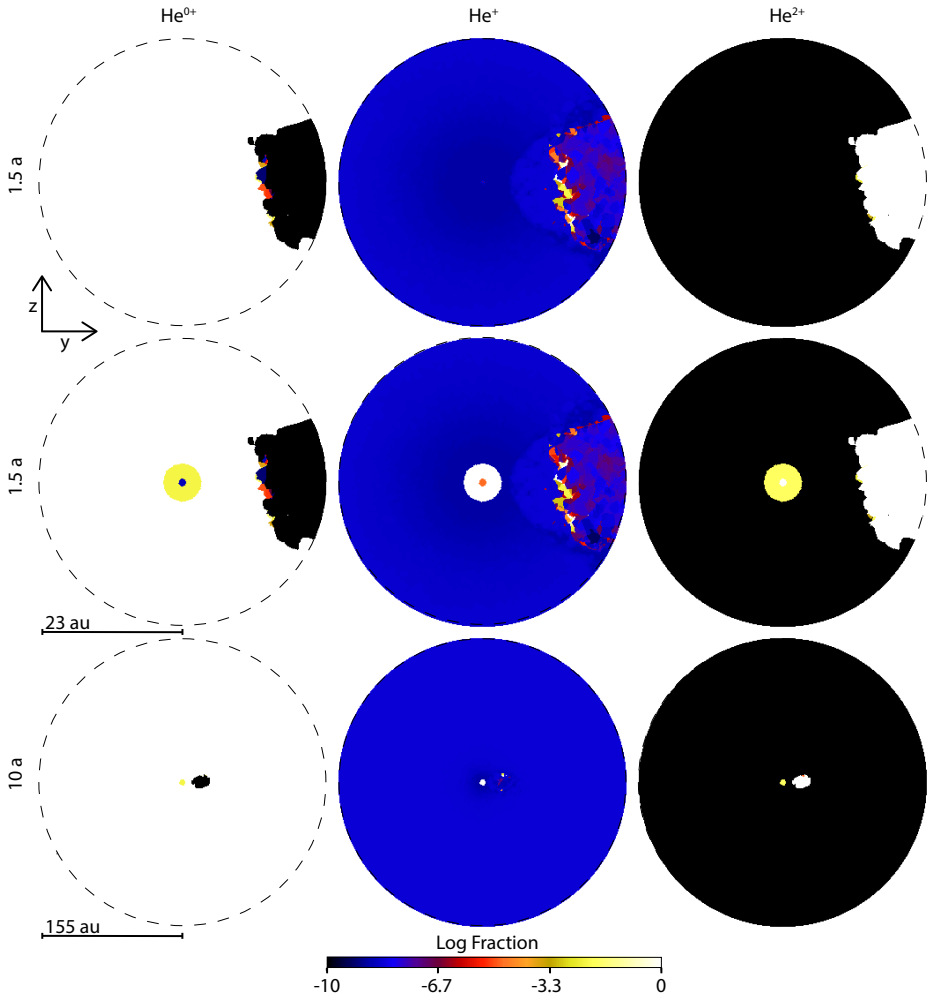

Figure 4.9 – Same as Figure 4.5 but for the *yz* plane.

in the remnant of the trailing arm of the WWIR is collisionally ionized to He^{2+}, while the colder unshocked η_B wind is composed of He^{+} that has not yet recombined.

Figure 4.9 shows that in this plane, for Case A, only the very hot gas in the WWIR is collisionally ionized, to He^{2+}. The ionization structure in the *yz*-plane in Case B (Figure 4.10) is a bit more complex. As in Case A, very hot gas in the WWIR is collisionally ionized to He^{2+}, but closer to η_A there also exists a volume of He^{+}. Inspection of Figure 4.4 reveals that this is primary wind material expanding into the η_B wind cavity that is photoionized by η_B. The bottom row of Figure 4.10 furthermore shows that η_B is able to ionize He to He^{+} in a layer of the dense post-shock η_A wind that borders the cavity of hot η_B wind (see the white oval line extending to the right in the bottom row middle

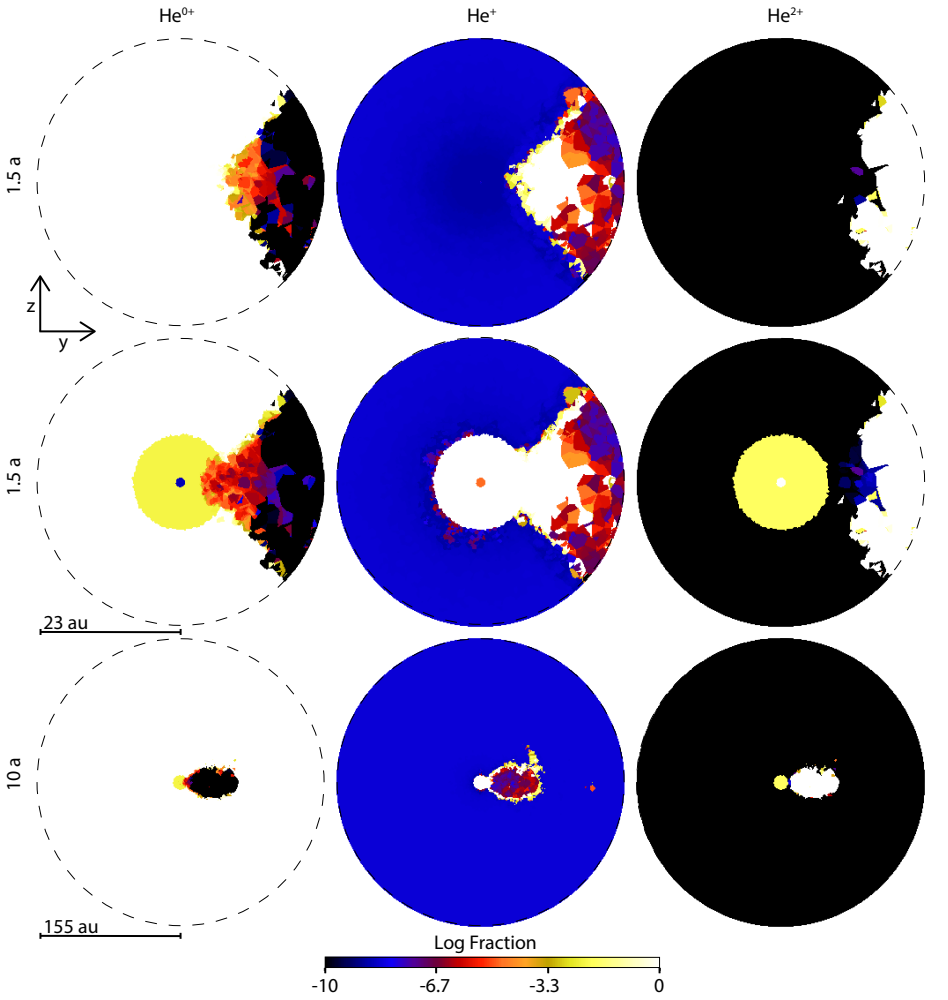

Figure 4.10 – Same as Figure 4.5 but for the Case B *yz* plane.

panel of Figure 4.10).

4.4 Discussion

From the discussions in Sections 4.2 and 4.3, it is evident that the interpretation of the results at periastron is much more difficult then at apastron, especially in terms of trying to understand how the results relate to observations of the various He line profiles (Nielsen et al. 2007; Damineli et al. 2008a). Nevertheless, we can use our results to try to better constrain the regions where the He emission and absorption features are generated. We focus on the Case A simulation results, since as discussed in M13, Chapters 3, and

above, they most likely better represent the current value of $\dot{M}_{\eta_A}$. We note that spectroscopic phase, defined by e.g. the disappearance of the narrow component of the He I lines (Damineli et al. 2008a, or alternatively, the minimum in the observed X-ray light curve, Corcoran et al. 2010), may differ from true orbital phase by up to one month.

Our results show that, at periastron, η_B is able to singly-ionize He in only a very thin layer of the post-shock η_A wind along the WWIR leading arm, and a very small region close to the stars. The denser η_A wind, expanding into the secondary wind cavity, is effectively able to stop the He^{0+}-ionizing photons. Therefore, the lower-density receding secondary wind on the apastron side and the adiabatically-cooling trailing arm of the WWIR from before periastron are shielded from ionizing photons from η_B. We do not expect this material to be neutral due to the long recombination time-scales for gas at these densities ($n < 10^7$) and temperatures ($\gtrsim 10^4$ K). The disappearance of the shock-heated region in the trailing arm of the WWIR, caused by the curvature of the WWIR, causes a strong asymmetry in the high temperature gas which is now mainly present in the WWIR leading arm. The He in this very hot region ($T > 10^6$ K) is collisionally doubly-ionized. With the exception of the inner He^+ and He^{2+} ionization regions due to η_A's ionizing flux, He in the extended primary wind is mostly neutral. This includes post-shock gas in the remnant of the trailing arm, and a significant portion of the extended leading arm, of the WWIR.

Observations show that the broad He I lines are generally blueshifted for most of the orbital period, both in emission and absorption. The P Cygni absorption starts increasing approximately three weeks before spectroscopic phase zero, reaching maximum absorption around phase zero, before decreasing to a complete disappearance ~ 20 days after phase zero (Nielsen et al. 2007; Damineli et al. 2008b). The radial velocity of the absorption reaches its maximum blueshifted value ($-610\,\mathrm{km\,s^{-1}}$) shortly before periastron, and then suddenly shifts during periastron down to $\sim -250\,\mathrm{km\,s^{-1}}$. This absorption must be produced by material between the observer and η_A, either in the WWIR or in the pre-shock wind of η_A.

Because the radial velocity variations seen in the He I λ7067 absorption are reminiscent of those observed from a star in a highly eccentric orbit, Nielsen et al. (2007) assumed that the He I absorption is associated with the pre-shock wind of η_A, ionized by the far-UV flux from η_B. However, this assumption leads to an unusual, extreme system mass ratio of $q \sim 0.1$, with a mass for η_B of 210 $M_\odot$ and a mass for η_A of ~ 20 $M_\odot$, in strong disagreement with the most commonly accepted values. In contrast, based on the maximum velocity of the absorption seen in the He I line and the requirements of high excitation flux and gas density, Damineli et al. (2008b) conclude that the only plausible locations for the formation of the broad He I absorptions are the walls of the WWIR. Our RT results favour this second scenario. At periastron, η_B is deep within the primary wind and its He^{0+}-ionizing photons are not able to reach the pre-shock η_A wind or penetrate beyond the dense layer of post-shock η_A wind. As shown in Figure 4.5 (central column, middle and bottom rows), He in the pre-shock primary wind is almost entirely neutral. The region of He^+ is confined to the centre of the system.

Modeling of η Car's X-ray light curve and observed broad, extended emission from numerous forbidden emission lines have helped constrain the orbital inclination (i), argument of periapsis (ω), and sky position angle (PA_z) of the η Car binary system (Okazaki et al. 2008; Parkin et al. 2009; Madura et al. 2012). It is generally agreed that the η Car binary is inclined away from the observer by roughly $\sim 45°$, with $\omega \approx 240°$–$285°$ and $PA_z \approx 302°$–$327°$, which places apastron on the observer's side of the system and implies that η_B orbits clockwise on the sky. With this orientation of the binary on the sky, at apastron, our line-of-sight (LOS) is more perpendicular to the apex of the WWIR surface. Based on the results in Chapters 3, we propose that the much denser WWIR (specifically, the compressed post-shock η_A wind) should dominate the P Cygni absorption at phases around apastron. However, because our LOS is more perpendicular to the WWIR around apastron, the column density of He^+ material between us and the continuum source η_A is relatively modest, resulting in a moderate amount of absorption. Moreover, because we are viewing the WWIR inclined away from us at roughly 45 degrees, material flowing toward us within the wall of post-shock η_A wind will have a maximum LOS velocity of $\sim 300\ km\,s^{-1}$, since the maximum true velocity of the gas within the compressed wall of post-shock η_A wind will be roughly equal to the terminal velocity of η_A's wind.

When approaching periastron, the trailing arm of the WWIR sweeps across our LOS. When this occurs, our LOS is parallel to and intersecting the WWIR. This results in a significantly increased column of He^+ between us and η_A, producing an increase in the amount of He I absorption. Because we are now looking directly down the WWIR, we are also seeing the fastest material in LOS, resulting not only in an increase in the amount of He I absorption, but also an increase in the blue-shifted velocity of this absorption. This scenario is in qualitative agreement with both the increase in the absorption and its shift toward more blue-shifted velocities of the observed He I P Cygni profiles going into periastron. Just after periastron, the strong He I λ7067 absorption component rapidly vanishes. This is also consistent with our results, since we see that at periastron, η_B is no longer able to ionize the WWIR or the primary wind. With the observer on the apastron side of the system, the gas in LOS, further away from the central region, cannot be ionized by η_B, resulting in effectively no He^+ between us and the central η_A He^+ region, and thus a lack of He I absorption.

Our results in Chapters 3 imply that the He I emission seen around apastron should arise from a combination of the inner η_A He^+ zone, the pre-shock η_A wind close to the WWIR apex that is ionized by η_B, and the layer of post-shock η_A wind in the WWIR that is also ionized by η_B. The different regions, depending on the orbital phase, where the He I emission can form might help explain the observed multiple emission components observed in the line profiles (Nielsen et al. 2007). At periastron, as discussed in M13, the WWIR apex is inside η_A's He^+ region. The fact that η_B is able to ionize an extremely small region close to the center of the system during periastron means that the dominant source of He I emission at periastron is the inner η_A He^+ region. Based on our models, little to no He I emission is expected from the WWIR at and just after periastron.

One other relevant result is connected with the formation of the He II λ4686 emission

line. Just before periastron, the He II λ4686 line intensity increases suddenly and then drops sharply to zero, after which it recovers to a second peak before declining back to zero (Steiner & Damineli 2004; Martin et al. 2006; Mehner et al. 2011; Teodoro et al. 2012). Based on the density and energy required for the formation of this line, the most plausible region in which it can form is close to the WWIR apex (Martin et al. 2006; Teodoro et al. 2012). Our results support the scenario proposed by M13 in which the He II λ4686 emission, observed at phases $\phi \sim 0.98$–1.3, is generated in the inner He^+ region of η_A's dense wind, with the necessary He^+-ionizing photons coming from the radiatively-cooling shocks in the WWIR. Our RT results show that, near periastron, η_B's ionizing flux is unable to produce a significant, extended region of He^+ in either the dense pre-shock η_A wind or the densest parts of the WWIR. Even though the unshocked η_B wind remains in the He^+ state during periastron, as discussed by e.g. Martin et al. (2006), Teodoro et al. (2012), the much lower-density η_B wind is incapable of adequately explaining the observed He II λ4686 emission. Thus, the only remaining region that can give rise to the observed He II λ4686 emission is the He^+ zone in η_A's dense inner wind.

The sharp drop in the He II λ4686 emission near periastron might be caused by a combination of two effects. First, we note that at periastron, the WWIR opening angle decreases considerably due to the much lower wind momentum ratio, caused by a large decrease in the pre-shock velocity of η_B's wind due to the decreased orbital separation and radiative inhibition effects (see Section 4.3 and M13). At periastron, η_B and the narrowed WWIR are also behind η_A and its optically-thick wind. Because the WWIR is much narrower, η_B and the WWIR are both 'eclipsed' by η_A and its dense wind at periastron. Second, if the WWIR 'collapses' at periastron due to the reduced η_B wind speed (see discussions in e.g. Corcoran et al. 2010, Parkin et al. 2011; M13), the radiatively-cooling WWIR shocks might disappear. If this occurs, the source of He^+-ionizing photons (i.e. the soft X-rays generated in the radiative shocks) necessary to produce the He II emission would also disappear. There would then obviously be no He II emission at periastron. We believe that a combination of a wind-eclipse by η_A and a 'collapse' of the WWIR is currently the best scenario for explaining the observed drop in He II λ4686 emission near periastron.

Finally, we briefly discuss the Case B simulation results, which show a similar behaviour to Case A, but with two major differences. The 1D CMFGEN models (Hillier et al. 2001, 2006) predict a radius for the inner He^+ region, due to η_A ionization, of ~ 7 au, more than a factor of two larger than in Case A. Even without this larger ionization region, η_B photons are able to ionize the denser primary wind, expanding into the η_B wind cavity, and reaching the expanding unshocked secondary wind on the apastron side of the system. Qualitatively, we expect these differences to produce variations, compared to Case A, both in the strength and velocity of the He emission and absorption lines. Moreover, the fact that η_B ionizing photons are still able at apastron to reach the periastron side of the system, have important implications on the phases at which these observed features occur. The increase in WWIR opening angle as $\dot{M}_{\eta_A}$ drops should also alter the timing of when specific He emission and absorption features are observed.

4.5 Summary and Conclusion

We presented the ionization structure of helium at periastron (i.e. the spectroscopic low state) in the inner regions of the η Car binary system due to the hot secondary star's ionizing flux. We created He ionization maps by post-processing 3D SPH simulations of the η Car system with SimpleX. Below we summarize our most important results and conclusions.

1. At periastron, the dense η_A wind expanding into the η_B wind cavity is able to stop η_B's He^{0+}-ionizing photons (in the Case A simulation). Helium is only singly-ionized by η_B in a very thin layer along the WWIR leading arm, and in a very small region close to the stars.

2. In Case B, the larger WWIR opening angle and lower $\dot{M}_{\eta_A}$ allow η_B to ionize a region of the lower-density unshocked η_B wind expanding in the apastron direction.

3. The inner He^+ volume due to η_A does not produce relevant differences in the final ionization structures due to η_B in simulation Case A. In Case B, the larger η_A He^+ radius allows the η_B ionizing photons to reach deeper into the dense η_A wind and create a lower ionization fraction in the pre-shock primary wind.

4. Collisional ionization creates He^{2+} in the hot shock-heated gas in the leading arm of the WWIR and in the adiabatically-cooling remnant of the trailing arm from just before periastron.

5. Our RT results support a binary orientation in which apastron is on the observer's side of the system, with the trailing arm of the WWIR sweeping across our LOS as periastron is approached.

6. The small He^+ region at the center of the system is the main region were He I emission can form during periastron. There is little to no He I absorption at periastron because η_B's ionizing flux is effectively trapped by η_A's dense wind, leading to a lack of dense He^+ gas between us and the continuum source η_A. This is consistent with the observed changes in strength and radial velocity of the He I P Cygni lines.

7. A lack of any significant He^+ in/near the WWIR at periastron, due to η_B, implies that the increased He II λ4686 emission that is observed around periastron must arise from the inner He^+ region in η_A's dense wind. Our results favour a scenario in which a combination of a wind-eclipse by η_A and a 'collapse' of the WWIR are responsible for the observed drop in He II λ4686 emission at periastron.

The He-ionization structures at periastron show a qualitative agreement with available observations of η Car's He lines. In the future, we plan to generate synthetic He line profiles for comparison to available observational data in order to place tighter constraints on the orbital, stellar, and wind parameters of η Car. These synthetic spectra, together

with those generated for the spectroscopic high state around apastron, will help us better understand the numerous observed spectral features generated in the inner ~ 150 au of the system. Our final aim is to use 3D time-dependent radiation-hydrodynamics simulations to more properly follow the ionization and recombination of the gas without post-processing. This is particularly important in the rapidly changing conditions and highly asymmetric situation at periastron.